Dalton Transactions

ROYAL SOCIETY OF CHEMISTRY

PAPER

View Article Online
View Journal | View Issue

Cite this: *Dalton Trans.*, 2025, **54**, 10599

Selective benzaldehyde/acetone to benzalacetone cross-aldol condensation catalyzed by UiO-66 MOFs†

Cesar Pazo-Carballo, [a,b,c] Esteban Camú, [b] Yoan Hidalgo-Rosa, [d,h] Jaime Llanos, [e] Ximena Zarate, [f] Ana Belén Dongil, [g] Eduardo Schott *[c] and Nestor Escalona *[a,b]

Cross-aldol condensation reactions are an important family of reactions that generate added-value chemicals with long chain products. Those products have multiple applications, such as those in the pharmaceutical industry, flavors and fragrances, agricultural chemicals and fine and specialty chemicals, among others. Possible products are long chain aromatic compounds, which could be used to generate fuels. The ability to generate that kind of fuel from biomass has been a challenge over the last few years. In this report the cross-aldol condensation reaction study using a family of UiO-66 MOFs between benzaldehyde and acetone to produce benzalacetone was performed. Thus, a family of UiO-66 MOFs was synthesized and characterized (by means of N_2 physisorption, NH_3-TPD, CO_2-TPD, ATR-FTIR, and powder X-ray diffraction) and its catalytic activity was studied in detail. Good conversion and selectivity were obtained. A thorough study of the kinetics of this reaction was performed for all the used UiO-66 MOFs. In this sense, the Langmuir–Hinshelwood kinetic models fitted the experimental data. The behavior predictions using different metals (Zr, Hf or Zr/Hf) and linkers (BDC or PDC) were fitted from the bimolecular one-site and two-site models. Competitive and non-competitive mechanisms were used to explain the production of the main intermediate compound (β-hydroxy ketone). The catalyst Zr/Hf-UiO-66 showed the best activity, which could be attributed to the greater total interaction energy of benzaldehyde/acetone on the catalyst surface (as shown by DFT calculations). A synergetic effect is observed for the bimetallic UiO-66 catalyst between Zr and Hf, obtaining a higher reaction rate than for the monometallic catalysts. Furthermore, a similar effect was reflected in the TOF for Zr/Hf-UiO-66. The best selectivity towards benzalacetone was obtained for Hf-UiO-66-PDC under iso-conversion conditions. Finally, depending on the metal–linker pair, differences in the benzaldehyde/acetone adsorption modes were observed, indicating the presence of bimolecular kinetic adjustments at one and two sites for the aldol condensation of benzaldehyde. All the results shown herein were supported by means of DFT calculations.

Received 27th February 2025,
Accepted 26th May 2025

DOI: 10.1039/d5dt00494b

rsc.li/dalton

1. Introduction

Metal–organic frameworks (MOFs) are hybrid molecules synthesized from metal ions and organic ligands (linkers) that form three-dimensional structures with high porosity and thermal and chemical stability.[1] Given the many combinations that can be made between metals and linkers, it is possible to develop MOFs with specific characteristics, which has allowed using these compounds for several years in different applications.[2,3]

A variety of catalytic reactions have been investigated using MOFs. Examples of organic chemical reactions that have been reported include condensation,[4] acetylations,[3] cycloaddition,[5] isomerization,[6] and hydrogenation.[6] Specific fine chemicals can be produced using MOF-based materials as effective cata-

[a]*Departamento de Química Física, Facultad de Química y Farmacia, Pontificia Universidad Católica de Chile, Chile. E-mail: neescalona@uc.cl*
[b]*Departamento de Ingeniería Química y Bioprocesos, Escuela de Ingeniería, Pontificia Universidad Católica de Chile, Chile*
[c]*Departamento de Química Inorgánica, Facultad de Química y de Farmacia, Pontificia Universidad Católica de Chile, Chile. E-mail: edschott@uc.cl, maschotte@gmail.com*
[d]*Centro de Nanotecnología Aplicada, Facultad de Ciencias, Ingeniería y Tecnología, Universidad Mayor, Santiago, Chile*
[e]*Departamento de Química, Facultad de Ciencias, Universidad Católica del Norte, Avda. Angamos 0610, Antofagasta 1270709, Chile*
[f]*Instituto de Ciencias Aplicadas, Facultad de Ingeniería, Universidad Autónoma de Chile, Chile*
[g]*Instituto de Catálisis y Petroleoquímica, CSIC, Cantoblanco, 28049 Madrid, España*
[h]*Escuela de Ingeniería del Medio Ambiente y Sustentabilidad, Facultad de Ciencias, Ingeniería y Tecnología, Universidad Mayor, Chile*

† Electronic supplementary information (ESI) available. See DOI: https://doi.org/10.1039/d5dt00494b

lysts.[7] Considering practical applications, recent research has focused on thermally and chemically stable MOFs, where Zr-MOFs are remarkably stable.[8,9] Due to their unique qualities, Zr-MOFs are valuable materials that make attractive candidates for heterogeneous catalysis, as catalysts or as supports for catalysts.[10] On the other hand, hafnium-based MOFs, which have outstanding thermal and chemical stability (similar to zirconium-based MOFs), have received considerably less attention. One of the frameworks that shows most of the previously mentioned characteristics corresponds to the UiO-66 MOF. UiO-66 (UiO = University of Oslo) consists of zirconium clusters ($Zr_6O_4(OH)_4$) as building units and organic linkers of 1,4-benzenedicarboxylate (BDC).[8] The metals or linkers could be changed, maintaining the MOF structure, but changing its properties (such as catalytic activity or porosity).[8]

It has been demonstrated that terephthalate defects are responsible for the UiO-66 material's catalytic activity in Lewis acid-catalyzed processes.[11,12] Furthermore, by replacing 1,4-benzenedicarboxylate with the 2,5-pyridinicarboxylate (PDC) ion linker, multiple isoreticular structures of UiO-66 may be produced. This would allow for the incorporation of more hydrophilic linker molecules, which would increase the amount of water that was absorbed by the reaction medium.[11,13–15] These modifications significantly alter the active site's characteristics and have an impact on the thermal and chemical stability. It was demonstrated by Lescouet *et al.*[16] that the catalytic activity can be tuned by replacing the linkers, which modifies the Brønsted acidity.

There are several reports of the catalytic activity in the UiO-66 MOF for reactions such as aldol condensation,[11] Knoevenagel condensation,[17] and Claisen–Schmidt condensation,[18] among others.

Aldol condensation is a widely used strategy to increase molecular size and generate added-value derivatives of biomass waste. Benzalacetone can be obtained from the reaction between benzaldehyde and acetone as a product. Benzalacetone has been shown to be essential in manufacturing added-value chemicals used in the pharmaceutical and food industries, as well as biofuels.[19] This reaction, particularly the benzaldehyde coupling condensation reaction, has been studied using homogeneous[20,21] and heterogeneous catalysts.[22,23] However, low yields and poor selectivity have been obtained.[22,23] Due to the MOF's versatility, these materials have been used as heterogeneous catalysts for this reaction in recent years.[24–26] The use of Zr-UiO-66 and Hf-UiO-66 as heterogeneous catalysts in aldol condensation has been investigated. However, no study has been performed on the electronic synergistic Zr/Hf interactions in the cluster and their impact on the catalytic performance of the process, as well as the influence of changing the hydrophilic character of the organic linkers containing PDC groups. To the best of our knowledge, the complete mechanism of the surface response has not yet been resolved. In addition, there is an ongoing need to generate novel and efficient catalysts to produce biofuels from biomass derivatives.

In this work, the cross-aldol condensation of benzaldehyde with acetone as a solvent-producing benzalacetone catalyzed by M-UiO-66-BDC (with M = Zr, Hf, and Zr/Hf) and M-UiO-66-PDC (with M = Zr and Hf) was carried out. Both families of MOFs were synthesized and characterized by N_2 physisorption using the BET Rouquerol method, NH_3-TPD, CO_2-TPD, ATR-FTIR, and powder X-Ray diffraction. The cross-aldol condensation reaction was studied in a batch reactor at 5.5 bar under N_2 and 383 K. Furthermore, DFT studies were carried out to support the catalytic results. Finally, the kinetics of the reaction was studied in detail fitting the experimental results with the bimolecular one and two site Langmuir–Hinshelwood (L–H) mechanisms.[27]

2. Experimental

2.1. Zr-, Hf-, and Zr/Hf-UiO-66-BDC synthesis

The three UiOs with BDC as the linker were synthesized using the procedure previously published by Farha *et al.*[28] A 20 mL vial was loaded with $ZrCl_4$ (125 mmol), 7.5 mL of DMF, and 1 mL of concentrated HCl before being sonicated for 20 minutes until fully dissolved. Finally, the linker (125 mmol) and another 7.5 mL of DMF were added, and the mixture was heated at 353 K overnight. In the case of the mixed metallic MOF (Zr/Hf-UiO-66-BDC), the metallic precursors $ZrCl_4$ and $HfCl_4$ were used in a 1 : 1 proportion (62.5 : 62.5 mmol).

2.2. Zr- and Hf-UiO-66-PDC synthesis

Zr- and Hf-UiO-66-PDC were prepared using Stock *et al.*[29] procedures (see the ESI† for further information). All products were separated and washed by centrifugation at 8000 rpm for 10 min with their solvent (2 × 10 mL) and then with ethanol (2 × 10 mL). Finally, the obtained solids were dried under vacuum at room temperature for five days.

2.3. Characterization of MOFs

The catalysts were characterized by N_2 physisorption, powder X-ray diffraction, temperature-programmed ammonia desorption (NH_3-TPD), temperature-programmed CO_2 desorption (CO_2-TPD), and infrared spectroscopy (more experimental details can be found in the ESI†).

2.4. Computational details

This study presents a series of calculations to explore the interactions between benzaldehyde and acetone with the material, *i.e.*, M-UiO-66-BDC or M-UiO-66-PDC. The interactions of acetone and benzaldehyde on material defect acidic sites have been investigated. Based on previous works discussed in the literature, the simulation was carried out by extracting a finite fragment of the MOFs (cluster model).[30] This method allows the simulation of a material's electronic properties through theoretical approaches and methodologies available in molecular software. In this report, a cluster model consistent with a single node $[M_6O_4(OH)_4]^{12-}$ was used (three complete linkers, seven truncated linkers, and considering only one defect or

vacancy).[31] To be more specific, the structure of the cluster model comprises the fragment $[M_6O_4(OH)_4(Linker)_3(HCOO)_8]$, with M representing Zr^{4+} and Hf^{4+}, while the linker refers to BDC or PDC. In contrast, one of the linker sites is vacant due to the consideration of a defect in the structure. Please refer to Fig. S1† for visual representation. The proposed structural model for the bi-metallic UiO-66 systems is composed of the fragment $[Zr_3Hf_3O_4(OH)_4(BDC)_3(HCOO)_8]$.

All calculations were carried out in the framework of the density-functional theory (DFT) method using the Amsterdam Density Functional (ADF 2023) software package.[32] The relativistic effects due to the presence of Zr or Hf can play a crucial role in the material's chemical and physical properties.[33] Thus, to consider the relativistic effects is essential for accurately describing a molecular properties. All simulations incorporated the relativistic effects using the zeroth-order regular approximation (ZORA).[34] The optimization of all structures was performed utilizing the Minnesota density M06-L functional,[35] along with the standard Slater-type orbital basis set and two additional polarization functions (STO-TZ2P).[36] In order to study the interaction between the systems M-UiO-66/acetone and M-UiO-66/benzaldehyde, the energy decomposition analysis (EDA) was employed using the Morokuma–Ziegler scheme.[37] The EDA analysis was performed using the *meta*-hybrid functional (10% HF exchange) by the Tao–Perdew–Staroverov–Scuseria TPSSH functional[37] at the TZ2P/ZORA level of theory. Eqn (1) demonstrates the breakdown of the interaction energy (ΔE_{Int}) in this analysis.

$$\Delta E_{Int} = \Delta E_{Pauli} + \Delta E_{Elec} + \Delta E_{Orb} + \Delta E_{Disp} \quad (1)$$

The term ΔE_{Pauli} accounts for the repulsive interaction between the occupied orbitals of both fragments.[38] The second term, ΔE_{Elec}, considers the traditional electrostatic interaction between the two fragments.[31] The third term, ΔE_{Orb}, encompasses interactions involving molecular orbitals associated with charge transfer, polarization, and other factors.[39] The term ΔE_{Disp} represents the contribution of dispersion force.[40] In this analysis, Grimme's D3 dispersion correction was employed to properly account for the dispersion forces in EDA computations.[41] This correction allows for the inclusion of weak interactions between the fragments. Furthermore, the analysis of orbital contribution was performed using the natural orbital of chemical valence (NOCV) approach introduced by Mitoraj.[42] The scheme considers the interaction of a system AB (with the wavefunction ψ AB) through the interaction of its individual fragments. NOCV analysis serves to identify the charge-flow channels, breaking down the overall change in density $\Delta\rho$. eqn (2) represents the NOCV by adding the total of pairs of complementary eigenfunctions (ψ_{-k}, ψ_k) associated with the eigenvalues ν_k and $-\nu_k$. The absolute values of these eigenvalues are equal, but their signs are opposite.[43]

$$\Delta\rho_{orb}(r) = \pi r^2(r) = \sum_{k=1}^{N/2} \Delta\rho_k \nu_k [-\psi_{-k}^2(r) + \psi_k^2(r)] = \sum_{k=1}^{N/2} \Delta\rho_k(r) \quad (2)$$

The molecular fragments establish charge-flow channels, which are determined by complementary pairs of NOCV. Within each $\Delta\rho_{orb}(i)$, electron density can be calculated for both outflow and inflow, denoted as $\Delta\rho_{orb}$ [outflow(i)] and $\Delta\rho_{orb}$ [inflow(i)], respectively. These calculations are based on pairs of NOCVs (ψ_{-k}, ψ_k) with identical absolute eigenvalues $|\nu_k|$. Eqn (4) allows for the examination of these terms individually. The focus is specifically on the processes of electron density outflow and inflow from a particular fragment.[38,44]

$$\Delta\rho_{orb}(r) = \sum_{k=1}^{N/2} \left[\Delta\rho_{orb}^{outflow}(i) + \Delta\rho_{orb}^{inflow}(i)\right] \quad (3)$$

The counterpoise approach was utilized to adjust the interaction energies due to the basis set superposition error (BSSE).[45]

2.5. Catalytic activities

UiO-66 (mono- and bimetallic) was activated before the catalytic test by drying the materials under vacuum at 453 K overnight in Micromeritics SmartVacPrep equipment. The aldol condensation was carried out at 383 K and 5.5 bar of nitrogen in a 20 mL batch reactor (Parr Model 4590) charged with 20 mg of the catalyst in 15 mL (247 mmol) of acetone, 0.60 mL of benzaldehyde and 0.445 mL (0.273 mmol) of *n*-dodecane as internal standards. The reaction mixture was then stirred at 700 rpm for four hours. Reaction conversion was monitored by taking aliquots (~200 μL) from the reaction mixture at different time intervals and analyzed by gas chromatography (GC) in a Shimadzu GC-2030 provided with a flame ionization detector (FID) equipped with an Elite-1 column (PerkinElmer, 30 m × 0.32 mm, film thickness: 0.25 μm). Conversion and product selectivity were defined according to eqn (4) and (5), respectively:

$$\text{Conversion}\,(\%) = \frac{n_{products}}{n_{reagent\ remaining} + n_{products}} \times 100 \quad (4)$$

$$\text{Selectivity}\,(\%) = \frac{n_{product\ i}}{\sum n_{products}} \times 100 \quad (5)$$

The initial reaction rate r_0 (mol g^{-1} s^{-1}) was calculated from the initial slope (b) of the conversion *vs.* time plot (s^{-1}) according to eqn (6), where m (g) represents the mass of the catalyst.

$$r_0 = \frac{b \times n^0_{benzaldehyde}}{m} \quad (6)$$

The mass balance was performed by comparing the conversion of benzaldehyde, indicated by its disappearance, with the generation of the analyzed products, showing a value superior to 80% in all the measurements.

2.6. Kinetic modeling

A rate expression that included the concentrations of benzaldehyde (Bal), benzalacetone (**B-One**), beta hydroxy acetone (**B-ol**), and acetone (Ac), based on the conventional bimolecular L–H one and two active site mechanisms, was used to

fit the experimental results. A nonlinear residual sum of squares (RSS) regression analysis of the differences between the observed and calculated values was used to provide the experimental data simultaneously. To ensure that the fitting resulted in the global minimum, different initial assumptions of the adjustable parameters ensured that the program always converged to the same minimum with the same fitting parameters for other initial guesses, as previously reported.[46]

3. Results and discussion

3.1. MOF characterization

The nitrogen isotherm exhibits the characteristic microporous structure type-I form according to the IUPAC report[47] (see Fig. S2 ESI†). The N_2 adsorption–desorption analysis allowed the evaluation of BET surface areas (S_{BET}) and total (V_t), mesoporous (V_m), and micropore volumes (V_0) of mono- and bimetallic UiO-66 catalysts, and these results are summarized in Table 1. The study of the textural properties of UiO-66-BDC revealed that all these materials presented similar BET surface areas. Additionally, Fig. S2 of the ESI† shows a change in the mesoporous zone of the isotherm for UiO-66-PDC due to the possible formation of mesopores or an interaction of the adsorbate–adsorbent with the free electron pairs of pyridinic nitrogen. According to the pore volume study, all mono- and bimetallic-UiO-66 MOFs have a total pore volume of more than 0.45 $cm^3\ g^{-1}$. A plot of the pore size distributions (PSDs) against pore width is shown in Fig. S3.† The PSDs for all UiO-66 synthesized were calculated by applying the NLDFT method from the desorption branch of the N_2 isotherms. Mono- and bimetallic UiO-66 MOFs displayed a pore distribution that corresponds to the two types of cavities present in the microporous structure of this material, which have been described as octahedral (≈11 Å) and tetrahedral (≈8 Å) cavities connected *via* triangular-shaped windows (≈6 Å), consistent with a previous report.[48] On the other hand, the pore size distribution of MOFs containing PDC is distorted. A reduction in the octahedral pore is found for Zr-UiO-66-PDC, but a broadening of the pores is reported for Hf-UiO-66. The nature of the synthesis probably causes textural alterations in both materials.

In order to evaluate the crystalline structure feature for all MOFs Fig. 1 shows the XRD patterns. According to the reference XRD pattern obtained by Cavka *et al.* and Camu *et al.*,[8,49]

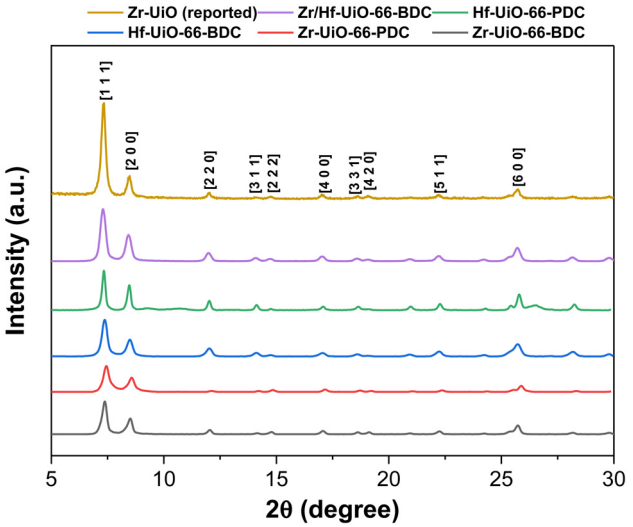

Fig. 1 XRD patterns obtained for UiO-66s.[8,49,50]

it was observed that all the materials present agreement in the diffraction patterns, suggesting a UiO-66 isostructural framework topology (fcu) for all the synthesized MOFs (mono- and bimetallic) in agreement with the literature.[49] Furthermore, an X-ray diffraction pattern of Zr-UiO-66 as a reference material was compared to that of the bimetallic Zr/Hf-UiO-66 sample to confirm that it displayed a pattern resembling that reported by Rogge *et al.*[50]

For the FT-IR spectroscopy study shown in Fig. S4,† the main differences between the structures are observed for the vibrations at 555, 660, and 740 cm^{-1} for mono- and bimetallic UiO-66 MOFs. These vibrations correspond to the μ_3–OH, μ_3–O and, M–OH bond stretching found in the secondary building unit (SBU) of each MOF.[51,52] The bands between 1506 and 1589 cm^{-1} correspond to the terephthalic acid ligands' C=C vibrational mode. The C–O stretching mode was allocated to the strong bands at ≈1393 cm^{-1}, and the distinctive band at ≈1664 cm^{-1} was attributed to the C=O vibrational mode in UiO-66. In addition, the produced PDC MOFs exhibit the disubstituted pyridine group's C=C vibrational mode, with vibrations between 1400 and 1594 cm^{-1}. Three weak bands linked to the pyridine's distinctive C–N bond can be observed between 1025 and 1200 cm^{-1}.

With the aim of determining the organic linker vacancies in the prepared MOFs, potentiometric acid–base titration and thermogravimetric analysis were performed; see Table S1.† All the studied MOFs showed linker vacancies, suggesting that all MOFs have high concentrations of acidic sites. The generation of acidic sites can be related to the inductive effect caused by the oxophilic nature of the metal cluster's atoms in the SBU. Additionally, at least three types of protons generated by water adsorption in the vacancies produced by the absence of the linker (μ_3–OH, –OH_2, and –OH) are observed in Fig. S5.†[53] Acid–base titration of both mono- and bimetallic UiO-66

Table 1 Textural properties of MOFs

Compound	S_{BET} ($m^2\ g^{-1}$)	V_0 ($cm^3\ g^{-1}$)	V_m ($cm^3\ g^{-1}$)	V_t ($cm^3\ g^{-1}$)
Zr-UiO-66-BDC	1377	0.51	0.08	0.59
Zr-UiO-66-PDC	1083	0.42	0.14	0.56
Zr/Hf-UiO-66-BDC	1325	0.51	0.06	0.57
Hf-UiO-66-BDC	934	0.38	0.12	0.46
Hf-UiO-66-PDC	601	0.16	0.29	0.45

reveals curves with three inflection points associated with the three types of protons. However, the defects or vacancies of 2,5-pyridinecarboxylate linkers were calculated using TGA, as reported by Valenzano *et al.*[54] showing that Zr-UiO-66-PDC presents the highest number of defects with respect to the other MOFs with a pyridine group in the linker molecule (Fig. S6 and S7†).

To get information about the type and nature of acidic sites over the different UiO-66 samples, temperature-programmed ammonia and carbon dioxide desorption was performed, followed by mass spectrometry (NH_3-TPD-MS and CO_2-TPD). The mass fragment 17 *m*/*z* was monitored while heating the MOFs from 100 to 450 °C, which indicates NH_3 binding to multiple sites. In Fig. S8a,† the behavior of NH_3 desorption temperature can be observed, demonstrating that all the catalysts displayed one single contribution according to maxima in the range from 124 to 254 °C. The distinct low-temperature desorption peak is attributed to NH_3 coordinated to weakly acidic sites of different TPD profiles.[55] After deconvolution of the NH_3 desorption peak (see Fig. S8b–f†), it was shown that MOFs using BDC as a linker include acidic sites below 150 °C, which might be ascribed to the creation of an NH_3 hydrogen bond in the μ_3–OH of the metal cluster. Above 150 °C, two peaks indicative of weakly acidic sites are detected. The overall quantity of acid in the heated MOFs and their derivatives may be represented as the amount of NH_3 bound to the acidic sites, which was calculated by subtracting the amount of physically adsorbed and hydrogen-bonded NH_3 from the total amount of NH_3. Table 2 shows the amounts of acidic sites for all MOFs, with a higher concentration observed for Zr/Hf-UiO-66 preceded by monometallic UiO-66. Regarding the MOFs with PDC as a linker, the presence of a fourth peak is observed, which could be attributed to the formation of a pyridinium ion resulting from the protonation of pyridinic nitrogen.

Fig. S9† depicts the CO_2 desorption patterns of all materials tested following activation at 180 °C. The desorbed quantities are presented in Table 2. A very modest CO_2 adsorption was observed for the conditions used for MOFs containing BDC. On the other hand, MOFs with PDC exhibit a distinct peak located around 115–150 °C with varying intensities and a weak shoulder at higher temperatures (185 °C). All materials showed weak basic sites with no distinction associated with the change of the organic linker.

Table 2 Concentration of total acidic and basic sites in MOFs determined by TPD-NH_3 and TPD-CO_2

Materials	Total acidic site amount (mmol g^{-1})	Total basic site amount (mmol g^{-1})
Zr-UiO-66-BDC	1.08	0.13
Hf-UiO-66-BDC	1.14	0.07
Zr/Hf-UiO-66-BDC	1.26	0.10
Zr-UiO-66-PDC	0.74	0.26
Hf-UiO-66-PDC	0.61	0.12

The XPS data provide details on the surface constituents of the material and the binding energies of the elements that make up the MOFs. Fig. S10† shows that Zr/Hf-UiO-66 contains Zr 3d, Hf 4f, C 1s and O 1s elements. The spectrum of Zr 3d has two Zr peaks ($3d_{3/2}$ and $3d_{5/2}$) located at 185.2 eV and 182.8 eV, respectively, indicating the existence of Zr^{4+} in O–Zr–O,[56] this being previously confirmed by FTIR-ATR. The Hf 4f spectra show two main peaks at binding energies of 17.5 and 19.1 eV, corresponding to the two Hf peaks ($4f_{7/2}$ and $4f_{5/2}$), respectively, whereas the three peaks found in the XPS spectrum of C 1s at 284.7, 286.5 and 288.8 eV are attributed to C–C, C═C and O–C–O groups, respectively. These types of bonds are characteristic of the carboxylate group and aromatic ring of the organic linker. The XPS spectrum of O 1s shows three main peaks located at 530.5, 532.1 and 533.5 eV; the first one is characteristic of metal–oxygen bonds and the other two are distinctive of oxygens corresponding to C═O and C–O bonds of the organic linker. The theoretical binding energies for Zr 3d and Hf 4f show values of 182.3 eV and 18.3 eV for the M–O bond, respectively. XPS analysis of bimetallic UiO-66 revealed an atomic ratio of almost 1 : 1 for Zr/Hf-UiO-66 (see Table S2†). This suggests that there are three Zr and three Hf atoms in the MOF metal cluster as reported in the literature.[8]

On the other hand, XPS analysis shows a small shift (>0.5 eV) for the binding energy of Zr 3d and Hf 4f present on the surface of bimetallic UiO-66 (see Fig. S10†). Evidence suggests an electronic interchange when both metals are present in the metal cluster of UiO-66. Therefore, it could improve the cooperative effect that allows for predicting an enhancement in catalytic activity.

3.2. Theoretical results

The M-UiO-66/**Bal** and M-UiO-66/**Ac** systems were initially studied using the host/guest interaction models (where **Bal** represents benzaldehyde and **Ac** corresponds to acetone). These models consider the interaction between the host (M-UiO-66) and the guest molecules (**Bal** or **Ac**) on defect sites generated by a missing linker. According to the results of the geometry optimization, it is observed that in the M-UiO-66-PDC or M-UiO-66-BDC systems, **Bal** and **Ac** exhibit a final conformation in closer proximity to the Lewis (M) and Brønsted (μ_3–O) acid sites. The optimized geometries of the Hf-UiO-66-BDC/**Bal** and Zr-UiO-66-BDC/**Bal** systems at the ground electronic state (S_0) can be seen in Fig. S11 of the ESI.† For these intermolecular interactions, the calculated lengths of Hf···OHC– and Zr···OHC– are 2.27 and 2.29 Å, for Hf-UiO-66-BDC/**Bal** and Zr-UiO-66-BDC/**Bal**, respectively; see Table S3.† For these systems, the angles of C–O···Hf and C–O···Zr are 142° and 130°, respectively, which are commonly found for the C═O···M interaction.[57] The Zr/Hf-UiO-66-BDC/**Bal** system exhibits optimized structures in the S_0 electronic state that closely resemble the arrangement found in the monometallic-UiO-66 systems. The bimetallic-UiO-66-BDC exhibits a geometric arrangement where the interacting system demonstrates that **Bal** interacts with the Hf metal center at the defective site. The intermolecular interaction is characterized by a Hf···OHC– dis-

tance of 2.27(0) Å and an angle of 141° between carbonyl groups of **Bal** and the Hf metal center of node; see Fig. S12.† Regarding the M-UiO-66-PDC/**Bal** systems, the orientation of the **Bal** molecules is such that the carbonyl groups face both the metal site (Hf or Zr) of the material and the N atoms of the PDC linker pyridine ring. The C–O···M interaction leads to intermolecular distances of 2.27 and 2.30 Å, with angles of 123° and 122° for Hf-UiO-66-PDC/**Bal** and Zr-UiO-66-PDC/**Bal**, respectively. As shown, the angles suffer a slight diminution in comparison with the BDC systems, which could be related to the presence of the N atom. Furthermore, the intermolecular contact between M-UiO-66-PDC and **Bal** through the N atom (N···HOC–) of 3.55 and 3.52 Å, accompanied by C–H···N angles of 162° and 163°, respectively, is displayed in Fig. S13.†

In the case of **Ac** interacting with Lewis (metal center) and Brønsted (μ_3–O) acid sites, similar effects are observed for the carbonyl group. Specifically, in the monometallic-UiO-66 system, the final conformation consisted of two intermolecular interactions. The first is the interaction of the **Ac** carbonyl group shifting to a position closer to the metal center in the defective sites. The second interaction forms a hydrogen bond between a methyl group hydrogen atom and a μ3–O site O atom. The bimetallic-UiO-66 system shows the **Ac** final conformation comparable to that of the monometallic-UiO-66/**Ac** system. However, in contrast to the Zr/Hf-UiO-66-BDC/**Bal** system, the **Ac** carbonyl group interaction is produced with the Zr metallic center in the defective site (see Fig. S12b†) and selected bond lengths for the monometallic-UiO-66/**Ac** systems are displayed in Fig. S14.† The estimated distance between the **Ac** carbonyl group and the material's metallic center, denoted as –C═O···M, is between 2.29 and 2.39 Å; see Fig. S14.† Additionally, the angle values range from 134 to 142°, as shown in Table S3,† which is in concordance with the previously described interaction angles. The calculated –C–H···μ_3–O hydrogen bond length is between 2.00 and 2.30 Å; see Fig. S14.† The [–C–H···μ_3–O] angle was in the range of 134 to 142° (see Table S3†).

To obtain a more comprehensive understanding of the intermolecular interactions between **Bal** and **Ac** molecules in the acidic sites of the material, the energy decomposition analysis (EDA) and the natural orbital of chemical valence (NOCV) methods were used. The EDA results indicate that the electrostatic factor plays a significant role in stabilizing energy in all systems. For instance, in the M-UiO-66-PDC/**Bal** and M-UiO-66-PDC/**Ac** systems, the ΔE_{Elec} component accounts for approximately 55 to 58% of the overall stabilizing energy, as shown in Table S4.† In the case of the M-UiO-66-BDC/**Bal** and M-UiO-66-BDC/Ac systems, about 45 to 50% of the overall stabilization is due to the ΔE_{Elec}. Besides, the calculations also indicated that orbital interactions play a significant role in the total stabilizing energy of all systems. It was observed that ΔE_{Orb} ranges from 33 to 42% for all systems. The ΔE_{Orb} refers to the stabilization energy resulting from the interaction of molecular orbitals between interacting species.

The results showed that **Bal** and **Ac** molecules might have a strong affinity for the acidic sites (Lewis and Brønsted) present in the studied mono- and bimetallic UiO-66 structures. The ΔE_{Orb} component was examined using the NOCV method to investigate the intermolecular interactions.[42,58] From the NOCV deformation density channel ($\Delta\rho_i$) it was found that both molecules (*i.e.* **Bal** and **Ac**) interact with a metallic center. Eqn (3) describes how the deformation density channels arising from NOCVs can be expressed as the movement of electron density out or into a specific fragment. The plots of deformation density ($\Delta\rho_1$), shown in Fig. S15–S18,† indicate the flow of charge from the molecules (**Bal** or **Ac**, outflow) to the metal center (inflow) in all systems. In these NOCV images the deformation density channels are represented by the reduction of electron density (outflow, red contours) and the accumulation of electron density (inflow, blue contours). Thus, in all systems, the main charge transfer channel $\Delta\rho_i$, evidences a charge flow from the carbonyl group oxygen atom lone pair of **Bal** or **Ac** to the MOF metal center. On the other hand, energetic estimations, $\Delta E_{Orb}(1)$, for each $\Delta\rho(1)$, account for 41 to 63% of the orbital component; see Table S3.† No evidence was found regarding the interaction between the molecule (**Bal** or **Ac**) and the Brønsted acid sites of the material when examining the remaining significant deformation density channels, $\Delta\rho_{orb}(i)$, based on their corresponding energy, $\Delta E_{Orb}(i)$. The analysis of all systems shows that the EDA-NOCV analysis uncovers the significance of Lewis sites in UiO-66's defective sites. These Lewis sites play a crucial role in the interactions between the adsorbate (**Bal** or **Ac**) and the adsorbent (UiO-66 material), which govern the adsorption mechanism of the **Bal–Ac** pair on the surface.

3.3. Catalytic activity

It has been described that the cross-aldol condensation between **Bal** and **Ac** produces C–C coupling. Therefore, acetone is deprotonated to form an enol or enolate-type nucleophile, and this generated intermediary molecule reacts with the carbonyl group of benzaldehyde (electrophile) to obtain a conjugated system of an α,β-unsaturated carbonyl as the final product. This reaction is interesting and important as it consists of two steps occurring *in situ*. First, α,β-hydroxyketone (**B-ol**) is formed according to the aldol reaction (see Fig. 2). Subsequently, a conjugated system of an α,β-unsaturated carbonyl corresponding to benzalacetone (see Fig. 2, **B-one**) is obtained as the final product produced due to the dehydration of **B-ol**. Previous reports of layered double hydroxides show a large conversion (around 100%), whereas a low selectivity, which does not get over 55%.[59,60] Furthermore, the use of NaOH as a homogeneous catalyst shows a large conversion and also a good conversion; however, the purification

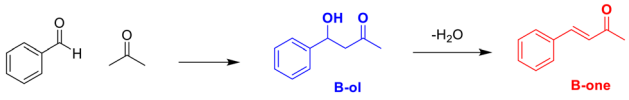

Fig. 2 Schematic reaction of cross-aldol condensation of benzaldehyde and acetone.

of **B-one** is complicated.[61] A similar catalyst (as in this report), constituted by the addition of Cs^+ over a β-zeolite has shown a conversion of 72% with a selectivity of 98%.[62]

The catalytic and selective activity of the herein-studied MOFs in the cross-condensation of benzaldehyde and acetone to produce benzalacetone changed as the organic linker was altered. Fig. 3a–c depict the catalytic conversion development of mono- and bi-metallic UiO-66 catalysts with 1,4-benzenedicarboxylic acid (BDC) as an organic linker. While Fig. 3d and e show the trend of catalytic activities based on cross-aldol condensation of benzaldehyde/acetone with 2,5-pyridinedicarboxylic acid (PDC) as an organic linker. Also, this figure illustrates the differences in initial material conversion as a function of time for the five MOFs under study. Every catalyst increases the conversion over time, which might explain the variations of the acid–base characteristics in each material. Also, the absence of a linker (defect) creates Lewis acid sites, like coordinatively unsaturated spots, which facilitate reagent adsorption. However, according to the physicochemical analysis, all defective UiO-66 sites have a variety of acidic sites that promote dynamic acidity throughout the condensation reaction. The production of enolate or enol intermediates during the aldol condensation depends on the presence of UiO-66 acid active sites. Furthermore, the presence of the free electron pair of nitrogen atoms in the MOF organic linker aromatic ring has a significant effect on each substance's acid–base characteristics. Similar to the previous results, some acetone auto-condensation reaction was observed when the bimetallic UiO-66 was used. However, the results obtained support the fact that the MOFs studied have a higher selectivity for the cross-coupling aldol condensation.

In addition, Fig. 4 presents the MOFs' catalytic activity concerning the turnover frequency (TOF) behavior calculated from the initial reaction rate normalized by the total acidic sites for each material used. The more significant amount of MOF acid sites might impact how benzaldehyde interacts with the MOF and how it is adsorbed onto surfaces. However, the diversity of total acidic sites among the remaining 5 MOFs produces differences in catalytic activities, which suggests coordinated active site kinetics. As there is no specific kinetic route to create benzalacetone, this concerted mechanism connected to the concentration of acid–base sites reduces the initial reaction rate.[63] The

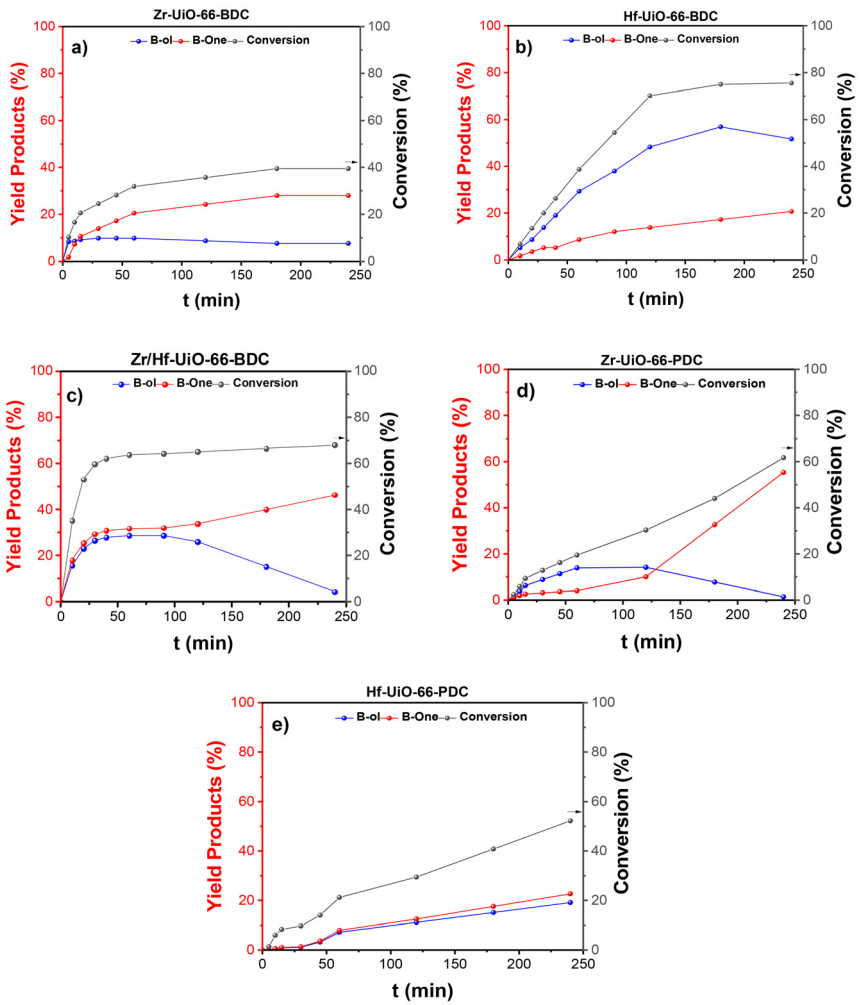

Fig. 3 Catalytic conversion over (a–c) mono- and bimetallic UiO-66-BDC, and (d–e) UiO-66-PDC *via* cross-coupling aldol condensation reaction.

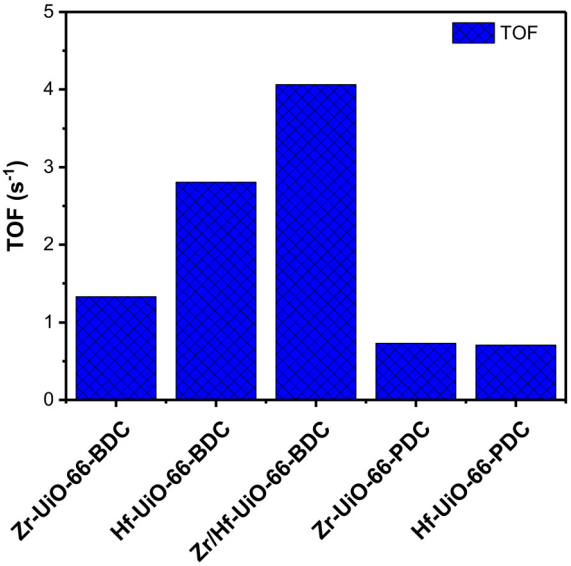

Fig. 4 Turnover-frequency as a function of total acid surface density of UiO-66 catalysts for cross-aldol condensation of benzaldehyde and acetone.

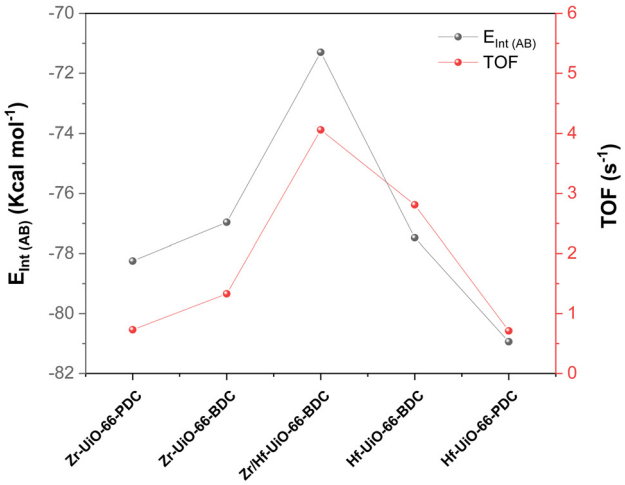

Fig. 5 Correlation between the turnover frequency and interaction energy for cross-aldol condensation (Bal/Ac) over MOFs.

catalytic environment of Zr/Hf-UiO-66 is more favorable for benzaldehyde conversion due to the formation of unique electronic and steric effects that influence the strength of the defect density in the MOF metal cluster. Concerning monometallic UiO-66, the interaction energy of the benzaldehyde on the material's surface is influenced by the oxophilic character of the metals in the SBU of MOFs, which leads to variations in the pace at which the target product forms. With a higher oxophilic character of the constituent metals of the SBU, an increase in the catalytic activity of the materials is expected. However, the presence of pyridinic groups in the organic ligand decreases the strength of the acidic sites in the metal clusters of MOFs, decreasing the catalytic activity toward C–C coupling formation.

The relevance of active sites in the material vacancies is shown by a comparative examination of the interaction energies acquired using EDA-NOCV analysis, and the catalytic activity determined using TOF. Specifically, the acidic sites play a key role in the interactions between the adsorbate (**Bal** or **Ac**) and the adsorbent (UiO-66 MOFs), influencing the **Bal–Ac** interaction process onto the surface. Fig. 5 depicts the trend of the total interaction energies of the **Bal–Ac** pair on the surface of each MOF *vs.* the calculated TOF for this reaction. The TOF describes the quantity of molecules of benzaldehyde converted into the specified product per second. Because of the metal composition in the cluster, Zr/Hf-UiO-66 has the highest TOF due to the cooperative effects of total acidity, defectivity, site availability, and electronic distribution, which are impacted by the catalyst's acidic site strength. In addition, this cooperative effect enhances the adsorption of the reactants (Bal–Ac) on the catalyst surface and consequently increases the possibility of the active site interactions with the reactants. Furthermore, the geometry optimization study reveals that Zr/Hf-UiO-66 has a distinct geometrical arrangement when interacting with **Bal** or **Ac**. Thus, the interacting system supports that **Bal** interacts preferentially with the Hf metal center at the defect site, whereas **Ac** interacts preferentially with Zr. Also, the main intermolecular interaction is given by an Hf···OHC– bond between the carbonyl groups of **Bal** and the Hf metal core of the node, as shown in Fig. S8a and S8b.†

Fig. 6 presents the selectivity behavior of all the MOFs under isoconversion conditions (30% of conversion), highlighting the variations in the β-hydroxyketone and benzalacetone concentrations. The differences in selectivity might be related to a modest variation in the active sites' nature of each catalyst and how these sites impact the intermolecular interaction geometry of the reactants on the catalyst's surface. As reported by Pazo *et al.*,[63] the water produced from aldol dehydration adsorbs on the catalyst surface, changing the nature

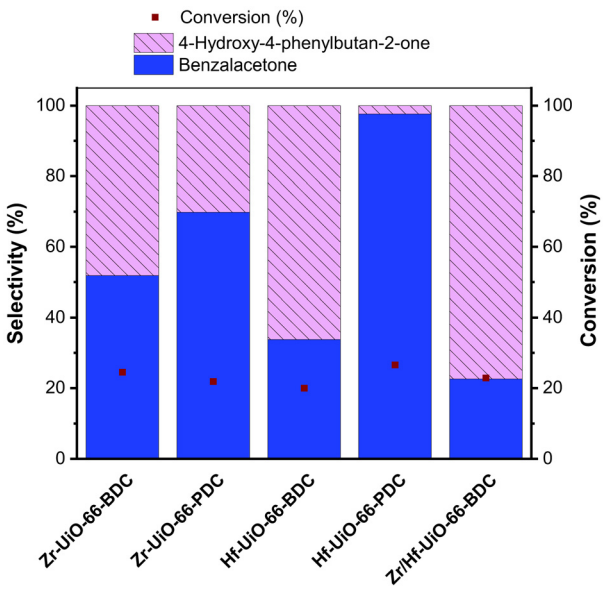

Fig. 6 Selectivity obtained at 20% conversion in UiO-66 catalysts.

of the acidic site. For this reason, UiO-66-BDC presents low selectivity towards the formation of the α,β-unsaturated carbonyl groups. According to the results obtained, both UiO-66-PDCs are more selective for cross-aldol condensation than MOFs containing the BDC linker, because the electron pair of the PDC offers an influence on the nature of the active site of the material. While the hydrogen atom connected to the oxo atom of the μ_3–OH group protonates the acetone's carbonyl, the PDC nitrogen's electron pair is expected to interact with the carbonyl carbon of the benzaldehyde. This behavior suggests that, in addition to the free electron pair of the pyridine nitrogen, the acetone–benzaldehyde couple interacts primarily with three types of protons that are present in the UiO-66-PDC structure: μ_3–OH, –OH_2, and –OH protons. The formation of hydrogen bonds and van der Waals-type interactions cause these interactions, which are somewhat consistent with the previously reported theoretical computations.

Finally, a process of **Ac** enolization by the abstraction of the protons facilitated by the acid–base pairs in the frameworks is presented by thermal analyses of the acidity and basicity of each material. According to a proposal made by Rojas *et al.*,[64,65] the metal center polarizes the acetone's carbonyl group. This polarization causes α-proton acidification, making its abstraction easier by the metal center's structural oxygen atom. The framework's bridging oxygen atom works as a base, creating an enolate. A combination of factors in Hf-UiO-66 has higher catalytic activity (Lewis's acidity, accessibility of active sites, pore volume, and surface contacts). A distinct behavior is observed when the pyridine groups are in the MOF's organic linker. Thus, the adsorption modes of the reagents on the active sites, as depicted in Fig. 7, indicate that the aldol condensation on UiO-66 with BDC and PDC exhibits different kinetic mechanisms depending on the metal and organic linker present in the MOF structure.

3.4. Kinetic modeling of UiO-66

The aldol condensation of benzaldehyde with acetone is generally acknowledged to be caused by the presence of a catalyst with acidic or basic properties.[11,65,66] Different possible reaction mechanisms were studied to understand further the cross-coupling condensation mechanism using UiO-66 as a catalyst. Thus, the UiO-66 catalytic reaction to generate benzalacetone involves six stages, according to the proposed reaction mechanism (Fig. 8a). This mechanism relies on the UiO-66 material's ability to possess catalytically active sites, which have been proposed to be generated during the synthesis of the material.[54] Specifically, the Lewis acid sites are generated due to the MOF's defect creation, resulting in coordinatively unsaturated sites.

The steps of the cross-aldol reaction depicted in Fig. 8a will be first discussed. According to the suggested Langmuir–Hinshelwood mechanism (LHM), both reagents are adsorbed through their carbonyl oxygen group on adjacent MOF metallic atoms (steps 7–8). The **Ac** molecule is activated by the α-carbon atom, inducing a hydrogen transfer to the metal cluster μ_3–oxygen. An enolate intermediate[67] is created in the process, which is stabilized due to the contact with the metal active site (step 8). Metal-bonded enolate has a high tendency to attack the adsorbed benzaldehyde. Afterwards, a new intermediary state is created after a nucleophilic attack at step 9 (producing C–C coupling). This step involves the breakage of the enolate linked to the metal. The C–C coupling product generates a more stable intermediate along the reaction pathway in step 9. The hydrogen attached to the μ_3–oxygen atom in step 9 protonates the C–C coupling product, creating the aldol product. The molecule is rearranged into the active site of the MOF, and the α-carbon atom is deprotonated. Then, the α-carbon atom protonates the metal cluster μ_3–oxygen atom (step 11). Then, the hydroxyl group is broken from the obtained intermediate, forming the primary product, benzalacetone (step 12). Based on the calculated kinetic constants, the product is released quickly. Subsequently, water is created during the aldol condensation processes while benzalacetone is kept in the reaction medium. Fig. 8b shows the adsorption of **Bal** and **Ac** on two active sites of different natures. Due to the oxophilic difference of the clusters' metals, the less acidic reagent (Ac) likely adsorbs on a more oxophilic metal (Hf) and *vice versa*, as suggested by theoretical calculations. According

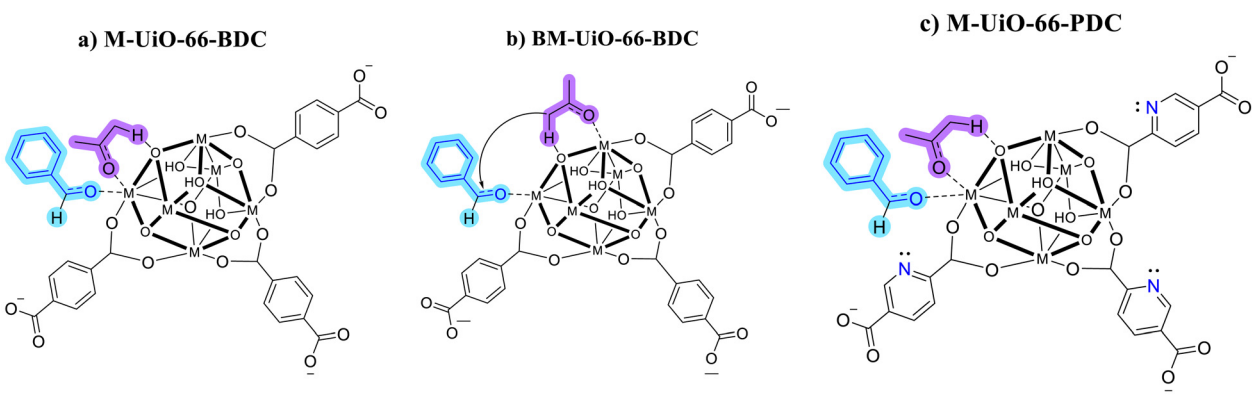

Fig. 7 Proposal of an adsorption mechanism of the benzaldehyde–acetone pair on the surfaces of (a) M-UiO-66-BDC, (b) Zr/Hf-UiO-66-BDC, and (c) M-UiO-66-PDC.

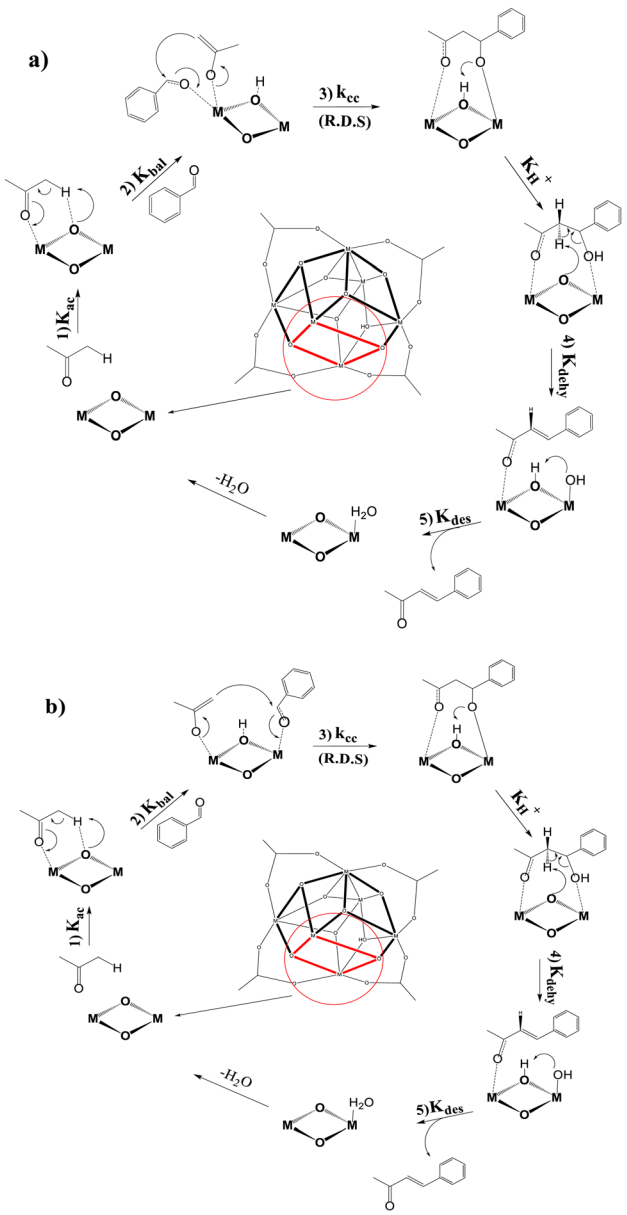

Fig. 8 Proposal of the surface reaction mechanism of UiO-66-BDC catalysts using the Langmuir–Hinshelwood model: (a) bimolecular one site and (b) bimolecular two sites.

to the above, bimolecular surface reaction mechanisms are proposed at one site when the MOF cluster is monometallic and at two sites when it is bimetallic.

It has been observed in the kinetic study that the determining step of the reaction is mainly associated with the subsequent protonation/deprotonation of the reactive molecules. The hydroxyl group is then dehydroxylated by chemisorption at the metal Lewis acid site. According to Pazo *et al.*, a modification to the catalytic site composition is suggested.[63] Accordingly, the elementary steps for benzaldehyde conversion can be described by the one-site L–H mechanism with the following equations, where "*" represents an active site, **Bol** is the reaction intermediate (beta hydroxy ketone), and **Bone** is the reaction product (benzalacetone).

$$\mathrm{Bal} + * \overset{K_{\mathrm{Bal}}}{\rightleftharpoons} \mathrm{Bal} - * \tag{7}$$

$$\mathrm{Ac} + * \overset{K_{\mathrm{Ac}}}{\rightleftharpoons} \mathrm{Ac} - * \tag{8}$$

$$\mathrm{Bal} - * + \mathrm{Ac} - * \xrightarrow{k_{\mathrm{cc}}} \mathrm{Bol} + 2* \ (\mathrm{rds}) \tag{9}$$

$$\mathrm{Bol} + * \overset{K_{\mathrm{Bol}}}{\rightleftharpoons} B - * \tag{10}$$

$$\mathrm{Bol} - * \overset{K_{\mathrm{dehy}}}{\rightleftharpoons} \mathrm{Bone} - * + \mathrm{H_2O} \tag{11}$$

$$\mathrm{Bone} - * \overset{K_{\mathrm{des}}}{\rightleftharpoons} \mathrm{Bone} + * \tag{12}$$

For the two sites, the L–H mechanism reaction steps involve the following equations:

$$\mathrm{Bal} + *_1 \overset{K_{\mathrm{Bal}}}{\rightleftharpoons} \mathrm{Bal} - *_1 \tag{13}$$

$$\mathrm{Ac} + *_2 \overset{K_{\mathrm{Ac}}}{\rightleftharpoons} \mathrm{Ac} - *_2 \tag{14}$$

$$\mathrm{Bal} - *_1 + \mathrm{Ac} - *_2 \xrightarrow{k_{\mathrm{cc}}} \mathrm{Bol} - *_1 + *_2 \ (\mathrm{rds}) \tag{15}$$

$$\mathrm{Bol} - *_1 \overset{K_{\mathrm{dehy}}}{\rightleftharpoons} \mathrm{Bone} - *_2 + \mathrm{H_2O} \tag{16}$$

$$\mathrm{Bone} - *_2 \overset{K_{\mathrm{des}}}{\rightleftharpoons} \mathrm{Bone} + *_2 \tag{17}$$

Under the reaction conditions, for the one-site and dual-site L–H mechanisms, the rate-determining step (RDS) is the surface reaction (eqn (9)). This step corresponds to the acetone and benzaldehyde adsorbed reaction to produce b-hydroxy ketone (eqn (9)), as the presence of **Bol** was revealed by gas chromatography. With these considerations, the rate expressions correspond to eqn (13) for one-site L–H and eqn (14) for a dual-site mechanism.

$$r = k_{\mathrm{cc}} K_{\mathrm{Bal}} K_{\mathrm{Ac}} [\mathrm{Bal}][\mathrm{Ac}] \theta_{\mathrm{v}}^2 \tag{18}$$

$$r = k_{\mathrm{cc}} K_{\mathrm{Bal}} K_{\mathrm{Ac}} [\mathrm{Bal}][\mathrm{Ac}] \theta_{\mathrm{v}_1} \theta_{\mathrm{v}_2} \tag{19}$$

where θ represents the fraction of surface area covered by each compound in the reaction, and the mathematical clearance of this model leads to the rate expression for the L–H (more details for both models can be found in the ESI†):

$$r = \frac{k_{\mathrm{cc}} K_{\mathrm{Bal}} K_{\mathrm{Ac}} [\mathrm{Bal}][\mathrm{Ac}]}{\left(1 + K_{\mathrm{bal}}[\mathrm{Bal}] + K_{\mathrm{Ac}}[\mathrm{Ac}] + K_{\mathrm{Bol}}[\mathrm{Bol}] + \dfrac{[\mathrm{Bone}]}{K_{\mathrm{des}}}\right)^2} \tag{20}$$

Then,

$$\theta_{\mathrm{v}} = \frac{1}{\left(1 + K_{\mathrm{bal}}[\mathrm{Bal}] + K_{\mathrm{Ac}}[\mathrm{Ac}] + K_{\mathrm{Bol}}[\mathrm{Bol}] + \dfrac{[\mathrm{Bone}]}{K_{\mathrm{des}}}\right)} \tag{21}$$

Simplifying the equations gives the following:

$$r = \frac{k'[\mathrm{Bal}][\mathrm{Ac}]}{\left(1 + K_{\mathrm{bal}}[\mathrm{Bal}] + K_{\mathrm{Ac}}[\mathrm{Ac}] + K_{\mathrm{Bol}}[\mathrm{Bol}] + \frac{[\mathrm{Bone}]}{K_{\mathrm{des}}}\right)^2} \quad (22)$$

$$r = \frac{k'[\mathrm{Bal}][\mathrm{Ac}]}{(1 + K_{\mathrm{bal}}[\mathrm{Bal}] + K_{\mathrm{Ac}}[\mathrm{Ac}])^2} \quad (23)$$

while for the two-site L–H model, the rate equation becomes:

$$r = \frac{k_{\mathrm{cc}} K_{\mathrm{Bal}} K_{\mathrm{Ac}}[\mathrm{Bal}][\mathrm{Ac}] L_1 L_2}{\left(1 + K_{\mathrm{Ac}}[\mathrm{Ac}] + \frac{[\mathrm{Bone}]}{K_{\mathrm{dehy}} K_{\mathrm{des}}} + \frac{[\mathrm{Bone}]}{K_{\mathrm{des}}}\right)(1 + K_{\mathrm{bal}}[\mathrm{Bal}])} \quad (24)$$

and

$$\theta_{v_1}\theta_{v_2} = \frac{L_1 L_2}{\left(1 + K_{\mathrm{Ac}}[\mathrm{Ac}] + \frac{[\mathrm{Bone}]}{K_{\mathrm{dehy}} K_{\mathrm{des}}} + \frac{[\mathrm{Bone}]}{K_{\mathrm{des}}}\right)(1 + K_{\mathrm{bal}}[\mathrm{Bal}])} \quad (25)$$

Simplifying the equations gives the following final equations:

$$r = \frac{k''[\mathrm{Bal}][\mathrm{Ac}]}{\left(1 + K_{\mathrm{Ac}}[\mathrm{Ac}] + \frac{[\mathrm{Bone}]}{K_{\mathrm{dehy}} K_{\mathrm{des}}} + \frac{[\mathrm{Bone}]}{K_{\mathrm{des}}}\right)(1 + K_{\mathrm{bal}}[\mathrm{Bal}])} \quad (26)$$

$$r = \frac{k''[\mathrm{Bal}][\mathrm{Ac}]}{(1 + K_{\mathrm{Ac}}[\mathrm{Ac}])(1 + K_{\mathrm{bal}}[\mathrm{Bal}])} \quad (27)$$

The results of adjustment of the kinetic models with experimental data are shown in Fig. S19.† Appreciably, the one-site L–H model best fits the experimental data, with an RSS value of >0.9976 when UiO-66 is monometallic with BDC as a linker and >0.9885 with PDC as an organic linker. The RSS value of the two-site L–H model is 0.9965 for Zr/Hf-UiO-66. This strongly suggests that the reaction is carried out by adsorbing **Bal** and **Ac**, as shown in Fig. 8a for the monometallic BDC MOFs. Both adsorbed **Bal** and **Ac** react by a nucleophilic attack of the enolate towards the benzaldehyde to generate **B-ol**. Finally, Table 3 shows the results of the kinetic parameters obtained from the bimolecular one-site L–H model. From the adsorption constant data, it is possible to establish that **Bal** and **Ac** have a greater affinity with the surface than the other compounds similar to that observed by DFT. This possibly explains why its generation was not observed during experimental analyses. Also, the adsorption constant for **Bone** is lower compared to the adsorption constant for the rest of the analyzed compounds, which favors the desorption of the product once **Bol** has been dehydrated on the surface of the catalyst. Moreover, in the bimolecular dual-site model, the rate limiting step is the attack of the enolate species by another **Ac** acting as an electrophile and adsorbed at a vicinal Lewis acid site, which facilitates the C–C coupling.

The same reaction mechanism was examined for the cross-aldol condensation found for UiO-66-PDC, which shows the importance of the presence of the oxo-atom in the inorganic piece as the basic site. Fig. 9 shows the proposed deprotonation of the acetone following adsorption on the Lewis acid site of the metal cluster in order to form the enolate by proton transfer from the α-carbon to the μ_3–oxygen. The pyridine group of the organic linker functions as an electron donor of the linker and does not actively participate in the reaction, and the effects of its presence on the various steps of the reaction profile appear to be minor. The linker's nature alters the reaction's kinetics due to the replacement of the phenyl group with the pyridine group, strengthening the benzaldehyde's contact, and forming a pseudo-hydrogen bridge connection.

Table 3 Optimized kinetic parameters obtained by fitting benzaldehyde and acetone condensation data on MOF catalysts with bimolecular Langmuir–Hinshelwood models

MOFs	Rate constant (mmol g^{-1} s^{-1}) k_{cc}	Adsorption equilibrium constant ($mmol^{-1}$) $K_{1(bal)}$	$K_{2(ac)}$	RSS	Model
Zr-UiO-66-BDC	1.059	0.1342	0.0089	0.9994	OSLH
Zr/Hf-UiO-66-BDC	19.638	0.0007	0.0303	0.9965	TSLH
Hf-UiO-66-BDC	3.809	0.0211	0.0915	0.9976	OSLH
Zr-UiO-66-PDC	3.669	0.0016	0.0034	0.9885	OSLH
Hf-UiO-66-PDC	4.926	0.0044	0.0219	0.9978	OSLH

OSLH: one site Langmuir–Hinshelwood model and TSLH: two site Langmuir–Hinshelwood model.

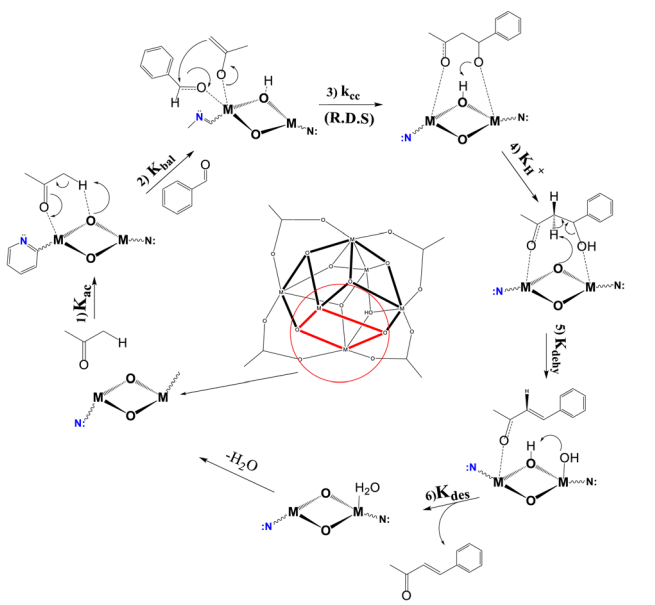

Fig. 9 Proposal of the surface reaction mechanism of UiO-66-PDC using the Langmuir–Hinshelwood model.

This contrasts with the findings of Hajek *et al.*,[12] who reported that using UiO-66 functionalized with an amino group resulted in slightly higher activity for cross-aldol formation due to slightly stronger adsorption. In summary, the adsorption of the reactants, combined with a slightly lower barrier for the pyridine-functionalized material, would point toward a lower catalytic activity.

Lastly, it has been noted that this catalytic process involves several variables, including acidic/basic sites, acid strength, pore volume, surface contacts, and active site accessibility that affect the kinetics of the reaction. It should be noted that the enhanced abilities of all MOFs to condense acetone with benzaldehyde and dehydrate the aldol intermediate to form the α,β-unsaturated carbonyl group exhibit desirable properties to be used in aldol condensation. Furthermore, Fig. S20† illustrates the Zr/Hf-UiO-66 catalyst's stability in relation to the production of benzalacetone. After the fifth repetition, the Zr/Hf-UiO-66 catalyst progressively loses its catalytic yield by around 17%, according to the results shown. In order to give an explanation for the loss in activity, XRD, surface area, FT-IR, TGA and XPS experiments were performed over the used catalyst. Fig. S21–25† show the obtained results. Textural and crystallography changes can be observed, which could support the collapse of some portions of the MOF. However, the microporosity and thermal stability are maintained. As can be observed in the XPS analysis, a slight composition change was observed on the surface of the material, which also supports some collapse of the MOF.

4. Conclusions

All the synthesized MOFs presented textural, crystalline, and acid–base characteristics according to the UiO-66 type materials. These MOFs were used in the catalytic experiments performed in this work. A higher initial catalytic activity was observed for the cross-aldol product, and benzaldehyde had a higher initial reaction rate with the MOF. Using Zr-UiO-66-BDC, Hf-UiO-66-BDC, and Zr/Hf-UiO-66-BDC, the reaction kinetics data were verified and compared with those of their corresponding UiO-66-PDC with Zr and Hf. However, the experiments predict a similar performance of both catalysts after four reaction hours. The total acidic sites play a crucial role in the interactions between the adsorbate (**Bal** or **Ac**) and the adsorbent (UiO-66 materials), which influence the Bal–Ac adsorption process on the surface. There is an observed trend between the DFT total interaction energies of the **Bal** and **Ac** pair on the surface of each MOF *vs.* the TOF. In all the catalysts, the experiment clearly shows a high selectivity towards the cross-product; however, in the parent UiO-66, there is competition with the self-aldol condensation in the very early phases of the reaction. The availability of active metal sites may also influence the activity ratio change of UiO-66 *vs.* UiO-66-PDC as a function of reaction time, although this needs more sophisticated approaches. Finally, the bimetallic UiO-66 presented a bimolecular kinetic adjustment of the two-site L–H model. In addition, as it is possible to appreciate, the one-site L–H model best fits the experimental data, with an RSS value of >0.9976 when the UiO-66 is monometallic with BDC as a linker and >0.9885 with PDC as an organic linker.

Data availability

The data supporting this article have been included as part of the ESI.†

Conflicts of interest

There are no conflicts to declare.

Acknowledgements

This work was supported by ANID-Chile under FONDECYT-Chile project 1241917, 1220763, 1231194, PIA CCTEAFB170007, ANID Post-doctoral 3230141, and FONDEQUIP EQM 160070. This work was also supported by FONDAP/SERC Chile/1523A0006. The authors are thankful for the financial support given by the European Commission through the H2020-MSCA-RISE-2020 BIOALL project (Grant Agreement: 101008058). Unidad de Equipamiento Científico MAINI®-XPS, ANID-FONDEQUIP EQM140044. This material is based upon work supported by the Air Force Office of Scientific Research under award number FA8655-25-1-8759.

References

1 V. V. Butova, M. A. Soldatov, A. A. Guda, K. A. Lomachenko and C. Lamberti, Metal–Organic Frameworks: Structure, Properties, Methods of Synthesis and Characterization, *Russ. Chem. Rev.*, 2016, **85**(3), 280–307, DOI: **10.1070/RCR4554**.
2 A. Herbst and C. Janiak, MOF Catalysts in Biomass Upgrading towards Value-Added Fine Chemicals, *CrystEngComm*, 2017, **19**(29), 4092–4117, DOI: **10.1039/c6ce01782g**.
3 D. Yang and B. C. Gates, Catalysis by Metal Organic Frameworks: Perspective and Suggestions for Future Research, *ACS Catal.*, 2019, **9**(3), 1779–1798, DOI: **10.1021/acscatal.8b04515**.
4 P. García-García, J. M. Moreno, U. Díaz, M. Bruix and A. Corma, Organic-Inorganic Supramolecular Solid Catalyst Boosts Organic Reactions in Water, *Nat. Commun.*, 2016, 10835, DOI: **10.1038/ncomms10835**.
5 V. L. Rechac, F. G. Cirujano, A. Corma and F. X. Llabrés i Xamena, Diastereoselective Synthesis of Pyranoquinolines on Zirconium-Containing UiO-66 Metal–Organic Frameworks, *Eur. J. Inorg. Chem.*, 2016, **2016**(27), 4512–4516, DOI: **10.1002/EJIC.201600372**.
6 M. Yabushita, P. Li, T. Islamoglu, H. Kobayashi, A. Fukuoka, O. K. Farha and A. Katz, Selective Metal-Organic Framework Catalysis of Glucose to 5-Hydroxymethylfurfural Using

Phosphate-Modified NU-1000, *Ind. Eng. Chem. Res.*, 2017, **56**(25), 7141–7148, DOI: 10.1021/ACS.IECR.7B01164/SUPPL_FILE/IE7B01164_SI_001.PDF.

7 A. Dhakshinamoorthy, M. Opanasenko, J. Čejka and H. Garcia, Metal Organic Frameworks as Heterogeneous Catalysts for the Production of Fine Chemicals, *Catal. Sci. Technol.*, 2013, **3**(10), 2509–2540, DOI: 10.1039/C3CY00350G.

8 J. H. Cavka, S. Jakobsen, U. Olsbye, N. Guillou, C. Lamberti, S. Bordiga and K. P. Lillerud, A New Zirconium Inorganic Building Brick Forming Metal Organic Frameworks with Exceptional Stability, *J. Am. Chem. Soc.*, 2008, **130**(42), 13850–13851, DOI: 10.1021/ja8057953.

9 H. Wu, T. Yildirim and W. Zhou, Exceptional Mechanical Stability of Highly Porous Zirconium Metal–Organic Framework UiO-66 and Its Important Implications, *J. Phys. Chem. Lett.*, 2013, **4**(6), 925–930, DOI: 10.1021/JZ4002345/SUPPL_FILE/JZ4002345_SI_006.CIF.

10 M. Rimoldi, A. J. Howarth, M. R. Destefano, L. Lin, S. Goswami, P. Li, J. T. Hupp and O. K. Farha, Catalytic Zirconium/Hafnium-Based Metal–Organic Frameworks, *ACS Catal.*, 2017, **7**(2), 997–1014, DOI: 10.1021/ACSCATAL.6B02923/ASSET/IMAGES/MEDIUM/CS-2016-02923U_0014.GIF.

11 F. Vermoortele, R. Ameloot and A. Vimont, An Amino-Modified Zr-Terephthalate Metal – Organic Framework as an Acid – Base Catalyst for Cross-Aldol Condensation, *Chem. Commun.*, 2011, 1521–1523, DOI: 10.1039/c0cc03038d.

12 J. Hajek, M. Vandichel, B. Van De Voorde, B. Bueken, D. De Vos, M. Waroquier and V. Van Speybroeck, Mechanistic Studies of Aldol Condensations in UiO-66 and UiO-66-NH2 Metal Organic Frameworks, *J. Catal.*, 2015, **331**, 1–12, DOI: 10.1016/j.jcat.2015.08.015.

13 Q. Yang, A. D. Wiersum, P. L. Llewellyn, V. Guillerm, C. Serre and G. Maurin, Functionalizing Porous Zirconium Terephthalate UiO-66(Zr) for Natural Gas Upgrading: A Computational Exploration, *Chem. Commun.*, 2011, **47**(34), 9603–9605, DOI: 10.1039/C1CC13543K.

14 M. Kandiah, S. Usseglio, S. Svelle, U. Olsbye, K. P. Lillerud and M. Tilset, Post-Synthetic Modification of the Metal–Organic Framework Compound UiO-66, *J. Mater. Chem.*, 2010, **20**(44), 9848–9851, DOI: 10.1039/C0JM02416C.

15 A. Cadiau, J. S. Lee, D. Damasceno Borges, P. Fabry, T. Devic, M. T. Wharmby, C. Martineau, D. Foucher, F. Taulelle, C.-H. Jun, Y. K. Hwang, N. Stock, M. F. De Lange, F. Kapteijn, J. Gascon, G. Maurin, J.-S. Chang and C. Serre, Design of Hydrophilic Metal Organic Framework Water Adsorbents for Heat Reallocation, *Adv. Mater.*, 2015, **27**(32), 4775–4780, DOI: 10.1002/adma.201502418.

16 T. Lescouet, C. Chizallet and D. Farrusseng, The Origin of the Activity of Amine-Functionalized Metal–Organic Frameworks in the Catalytic Synthesis of Cyclic Carbonates from Epoxide and CO2, *ChemCatChem*, 2012, **4**(11), 1725–1728, DOI: 10.1002/CCTC.201200288.

17 V. N. Panchenko, M. M. Matrosova, J. Jeon, J. Won Jun, M. N. Timofeeva and S. H. Jhung, Catalytic Behavior of Metal–Organic Frameworks in the Knoevenagel Condensation Reaction, *J. Catal.*, 2014, 251, DOI: 10.1016/j.jcat.2014.05.018.

18 A. Dhakshinamoorthy, M. Opanasenko, J. Čejka and H. Garcia, Metal Organic Frameworks as Solid Catalysts in Condensation Reactions of Carbonyl Groups, *Adv. Synth. Catal.*, 2013, **355**(2–3), 247–268, DOI: 10.1002/adsc.201200618.

19 D. Li, F. Shi, J. Peng, S. Guo and Y. Deng, Application of Functional Ionic Liquids Possessing Two Adjacent Acid Sites for Acetalization of Aldehydes, *J. Org. Chem.*, 2004, **69**(10), 3582–3585, DOI: 10.1021/jo034859l.

20 G. K. Baio Ferreira, C. Carvalho and S. Nakagaki, Studies of the Catalytic Activity of Iron(III) Porphyrins for the Protection of Carbonyl Groups in Homogeneous Media, *Catalysts*, 2019, **9**(4), 334, DOI: 10.3390/catal9040334.

21 M. M. Antunes, T. R. Amarante, A. A. Valente, F. A. Almeida Paz, I. S. Goncalves and M. Pillinger, A Linear Trinuclear Oxidodiperoxido-Molybdenum(VI) Complex with Single Triazole Bridges: Catalytic Activity in Epoxidation, Alcoholysis, and Acetalization Reactions, *ChemCatChem*, 2018, **10**(13, SI), 2782–2791, DOI: 10.1002/cctc.201800232.

22 A. L. G. Pinheiro, J. V. C. do Carmo, D. C. Carvalho, A. C. Oliveira, E. Rodríguez-Castellón, S. Tehuacanero-Cuapa, L. Otubo and R. Lang, Bio-Additive Fuels from Glycerol Acetalization over Metals-Containing Vanadium Oxide Nanotubes (MeVOx-NT in Which, Me = Ni, Co, or Pt), *Fuel Process. Technol.*, 2019, **184**, 45–56, DOI: 10.1016/j.fuproc.2018.11.008.

23 M.-S. Hosseini and M. Masteri-Farahani, Surface Functionalization of Magnetite Nanoparticles with Sulfonic Acid and Heteropoly Acid: Efficient Magnetically Recoverable Solid Acid Catalysts, *Chem. – Asian J.*, 2019, **14**(7), 1076–1083, DOI: 10.1002/asia.201801810.

24 U. S. F. Arrozi, H. W. Wijaya, A. Patah and Y. Permana, Efficient Acetalization of Benzaldehydes Using UiO-66 and UiO-67: Substrates Accessibility or Lewis Acidity of Zirconium, *Appl. Catal., A*, 2015, **506**, 77–84, DOI: 10.1016/j.apcata.2015.08.028.

25 P. Wang, J. Feng, Y. Zhao, S. Wang and J. Liu, MOF-Derived Tungstated Zirconia as Strong Solid Acids toward High Catalytic Performance for Acetalization, *ACS Appl. Mater. Interfaces*, 2016, **8**(36), 23755–23762, DOI: 10.1021/acsami.6b08057.

26 S.-S. Mortazavi, A. Abbasi, M. Masteri-Farahani and F. Farzaneh, Sulfonic Acid Functionalized MIL-101(Cr) Metal–Organic Framework for Catalytic Production of Acetals, *ChemistrySelect*, 2019, **4**(25), 7495–7501, DOI: 10.1002/slct.201901070.

27 C. N. Hinshelwood, The Kinetics of Chemical Change in Gaseous Systems, *Nature*, 1927, **119**(3004), 771–773, DOI: 10.1038/119771a0.

28 M. J. Katz, Z. J. Brown, Y. J. Colón, P. W. Siu, K. A. Scheidt, R. Q. Snurr, J. T. Hupp and O. K. Farha, A Facile Synthesis of UiO-66, UiO-67 and Their Derivatives, *Chem. Commun.*, 2013, **49**(82), 9449–9451, DOI: 10.1039/c3cc46105j.

29 S. Waitschat, D. Fröhlich, H. Reinsch, H. Terraschke, K. A. Lomachenko, C. Lamberti, H. Kummer, T. Helling, M. Baumgartner, S. Henninger and N. Stock, Synthesis of M-UiO-66 (M = Zr, Ce or Hf) Employing 2,5-Pyridinedicarboxylic Acid as a Linker: Defect Chemistry, Framework Hydrophilisation and Sorption Properties, *Dalton Trans.*, 2018, **47**(4), 1062–1070, DOI: 10.1039/c7dt03641h.

30 J. L. Mancuso, A. M. Mroz, K. N. Le and C. H. Hendon, Electronic Structure Modeling of Metal–Organic Frameworks, *Chem. Rev.*, 2020, **120**(16), 8641–8715, DOI: 10.1021/acs.chemrev.0c00148.

31 C. Pazo-Carballo, E. Blanco, E. Camu, A. Leiva, Y. Hidalgo-Rosa, X. Zarate, A. B. Dongil, E. Schott and N. Escalona, Theoretical and Experimental Study for Cross-Coupling Aldol Condensation over Mono- and Bimetallic UiO-66 Nanocatalysts, *ACS Appl. Nano Mater.*, 2023, **6**(7), 5422–5433, DOI: 10.1021/acsanm.2c05555.

32 G. te Velde, F. M. Bickelhaupt, E. J. Baerends, C. Fonseca Guerra, S. J. A. van Gisbergen, J. G. Snijders and T. Ziegler, Chemistry with ADF, *J. Comput. Chem.*, 2001, **22**(9), 931–967, DOI: 10.1002/jcc.1056.

33 M. Atanasov, D. Aravena, E. Suturina, E. Bill, D. Maganas and F. Neese, First Principles Approach to the Electronic Structure, Magnetic Anisotropy and Spin Relaxation in Mononuclear 3d-Transition Metal Single Molecule Magnets, *Coord. Chem. Rev.*, 2015, **289–290**(1), 177–214, DOI: 10.1016/j.ccr.2014.10.015.

34 E. Van Lenthe, E. J. Baerends, J. G. Snijders, E. Van Lenthe, E. J. Baerends and J. G. Snijders, Relativistic Regular Twocomponent Hamiltonians Relativistic Regular Two-Component Hamiltonians, *J. Chem. Phys.*, 1993, **99**(6), 4597–4610, DOI: 10.1063/1.466059.

35 Y. Zhao and D. G. Truhlar, A New Local Density Functional for Main-Group Thermochemistry, Transition Metal Bonding, Thermochemical Kinetics, and Noncovalent Interactions, *J. Chem. Phys.*, 2006, **125**(19), 194101, DOI: 10.1063/1.2370993.

36 E. Van Lenthe and E. J. Baerends, Optimized Slater-Type Basis Sets for the Elements 1–118, *J. Comput. Chem.*, 2003, **24**(9), 1142–1156, DOI: 10.1002/jcc.10255.

37 J. Tao, J. P. Perdew, V. N. Staroverov and G. E. Scuseria, Climbing the Density Functional Ladder: Nonempirical Meta–Generalized Gradient Approximation Designed for Molecules and Solids, *Phys. Rev. Lett.*, 2003, **91**(14), 3–6, DOI: 10.1103/PhysRevLett.91.146401.

38 F. Sagan and M. P. Mitoraj, Kinetic and Potential Energy Contributions to a Chemical Bond from the Charge and Energy Decomposition Scheme of Extended Transition State Natural Orbitals for Chemical Valence, *J. Phys. Chem. A*, 2019, **123**(21), 4616–4622, DOI: 10.1021/acs.jpca.9b01420.

39 M. P. Mitoraj, A. Michalak and T. Ziegler, A Combined Charge and Energy Decomposition Scheme for Bond Analysis, *J. Chem. Theory Comput.*, 2009, **5**(4), 962–975, DOI: 10.1021/ct800503d.

40 S. Grimme, J. Antony, S. Ehrlich and H. Krieg, A Consistent and Accurate Ab Initio Parametrization of Density Functional Dispersion Correction (DFT-D) for the 94 Elements H-Pu, *J. Chem. Phys.*, 2010, **132**(15), 5585, DOI: 10.1063/1.3382344.

41 S. Grimme, Density Functional Theory with London Dispersion Corrections, *Wiley Interdiscip. Rev.:Comput. Mol. Sci.*, 2011, **1**(2), 211–228, DOI: 10.1002/wcms.30.

42 M. P. Mitoraj, Bonding in Ammonia Borane: An Analysis Based on the Natural Orbitals for Chemical Valence and the Extended Transition State Method (ETS-NOCV), *J. Phys. Chem. A*, 2011, **115**(51), 14708–14716, DOI: 10.1021/jp209712s.

43 M. P. Mitoraj, A. Michalak and T. Ziegler, On the Nature of the Agostic Bond between Metal Centers and β-Hydrogen Atoms in Alkyl Complexes. An Analysis Based on the Extended Transition State Method and the Natural Orbitals for Chemical Valence Scheme (ETS-NOCV), *Organometallics*, 2009, **28**(13), 3727–3733, DOI: 10.1021/om900203m.

44 K. Devi, S. M. N. V. T. Gorantla and K. C. Mondal, EDA-NOCV Analysis of Carbene-Borylene Bonded Dinitrogen Complexes for Deeper Bonding Insight: A Fair Comparison with a Metal–Dinitrogen System, *J. Comput. Chem.*, 2022, **43**(11), 757–777, DOI: 10.1002/jcc.26832.

45 S. F. Boys and F. Bernardi, The Calculation of Small Molecular Interactions by the Differences of Separate Total Energies. Some Procedures with Reduced Errors, *Mol. Phys.*, 1970, **19**(4), 553–566, DOI: 10.1080/00268977000101561.

46 M. A. Vannice, *Kinetics of Catalytic Reactions*, Springer New York, NY, New York, 1st edn, 2005. DOI: 10.1007/b136380.

47 K. S. W. Sing, D. H. Everett, R. A. W. Haul, L. Moscou, R. A. Pierotti, J. Rouquerol and T. Siemieniewska, Reporting Physisoption Data for Gas/Solid Systems with Special Reference to the Determination of Surface Area and Porosity, *Pure Appl. Chem.*, 1985, **57**(4), 603–619.

48 Y. Han, M. Liu, K. Li, Y. Zuo, Y. Wei, S. Xu, G. Zhang, C. Song, Z. Zhang and X. Guo, Facile Synthesis of Morphology and Size-Controlled Zirconium Metal–Organic FrameworkUiO-66: The Role of Hydrofluoric Acid in Crystallization, *CrystEngComm*, 2015, **17**, 6434, DOI: 10.1039/c5ce00729a.

49 E. Camu, C. Pazo, D. Becerra, Y. Hidalgo-Rosa, D. Paez-Hernandez, X. Zarate, E. Schott and N. Escalona, A New Approach to the Mechanism for the Acetalization of Benzaldehyde over MOF Catalysts †, *New J. Chem.*, 2020, **44**, 14865, DOI: 10.1039/d0nj02416c.

50 S. M. J. Rogge, P. G. Yot, J. Jacobsen, F. Muniz-Miranda, S. Vandenbrande, J. Gosch, V. Ortiz, I. E. Collings, S. Devautour-Vinot, G. Maurin, N. Stock and V. Van

Speybroeck, Charting, the Metal–Dependent High-Pressure Stability of Bimetallic UiO-66 Materials, *ACS Mater. Lett.*, 2020, **2**(4), 438–445, DOI: **10.1021/acsmaterialslett.0c00042**.

51 M. Lammert, M. T. Wharmby, S. Smolders, B. Bueken, A. Lieb, K. A. Lomachenko, D. de Vos and N. Stock, Cerium-Based Metal Organic Frameworks with UiO-66 Architecture: Synthesis, Properties and Redox Catalytic Activity, *Chem. Commun.*, 2015, **51**(63), 12578–12581, DOI: **10.1039/C5CC02606G**.

52 L. Valenzano, B. Civalleri, S. Chavan, S. Bordiga, M. H. Nilsen, S. Jakobsen, K. P. Lillerud and C. Lamberti, Disclosing the Complex Structure of UiO-66 Metal Organic Framework: A Synergic Combination of Experiment and Theory, *Chem. Mater.*, 2011, **23**, 1700–1718, DOI: **10.1021/cm1022882**.

53 M. R. Destefano, T. Islamoglu, S. J. Garibay, J. T. Hupp and O. K. Farha, *Room-Temperature Synthesis of UiO-66 and Thermal Modulation of Densities of Defect Sites*. 2017. DOI: **10.1021/acs.chemmater.6b05115**.

54 L. Valenzano, B. Civalleri, S. Chavan, S. Bordiga, M. H. Nilsen, S. Jakobsen, K. P. Lillerud and C. Lamberti, Disclosing the Complex Structure of UiO-66 Metal Organic Framework: A Synergic Combination of Experiment and Theory, *Chem. Mater.*, 2011, **23**(7), 1700–1718, DOI: **10.1021/cm1022882**.

55 N. Y. Topsøe, K. Pedersen and E. G. Derouane, Infrared and Temperature-Programmed Desorption Study of the Acidic Properties of ZSM-5-Type Zeolites, *J. Catal.*, 1981, **70**(1), 41–52, DOI: **10.1016/0021-9517(81)90315-8**.

56 X. Jiang, S. Li, S. He, Y. Bai and L. Shao, Interface Manipulation of CO2—Philic Composite Membranes Containing Designed UiO-66 Derivatives towards Highly Efficient CO2 Capture, *J. Mater. Chem. A*, 2018, **6**(31), 15064–15073, DOI: **10.1039/C8TA03872D**.

57 M. Asgari, S. Jawahery, E. D. Bloch, M. R. Hudson, R. Flacau, B. Vlaisavljevich, J. R. Long, C. M. Brown and W. L. Queen, An Experimental and Computational Study of CO2 Adsorption in the Sodalite-Type M-BTT (M = Cr, Mn, Fe, Cu) Metal–Organic Frameworks Featuring Open Metal Sites, *Chem. Sci.*, 2018, **9**(20), 4579–4588, DOI: **10.1039/c8sc00971f**.

58 M. P. Mitoraj and A. Michalak, Theoretical Description of Halogen Bonding - An Insight Based on the Natural Orbitals for Chemical Valence Combined with the Extended-Transition- State Method (ETS-NOCV), *J. Mol. Model*, 2013, **19**(11), 4681–4688, DOI: **10.1007/s00894-012-1474-4**.

59 I. Paterová, E. Vyskočilová and L. Červený, Two-Step Preparation of Benzylacetone, *Top. Catal.*, 2012, **55**(11–13), 873–879, DOI: **10.1007/s11244-012-9853-8**.

60 K. K. Rao, M. Gravelle, J. S. Valente and F. Figueras, Activation of Mg–Al Hydrotalcite Catalysts for Aldol Condensation Reactions, *J. Catal.*, 1998, **173**(1), 115–121, DOI: **10.1006/jcat.1997.1878**.

61 R. Sun, C. Han and J. Xu, A Green Synthesis Approach toward Large-Scale Production of Benzalacetone *via* Claisen–Schmidt Condensation, *RSC Adv.*, 2022, **12**(45), 29240–29245, DOI: **10.1039/D2RA05320A**.

62 S. Ghosh, S. S. Acharyya, Y. Yoshida, T. Kaneko, Y. Iwasawa and T. Sasaki, Nontraditional Aldol Condensation Performance of Highly Efficient and Reusable Cs^+ Single Sites in β-Zeolite Channels, *ACS Appl. Mater. Interfaces*, 2022, **14**(16), 18464–18475, DOI: **10.1021/acsami.2c01312**.

63 C. Pazo-Carballo, E. Blanco, E. Camu, A. Leiva, Y. Hidalgo-Rosa, X. Zarate, A. B. Dongil, E. Schott and N. Escalona, Theoretical and Experimental Study for Cross-Coupling Aldol Condensation over Mono- and Bimetallic UiO-66 Nanocatalysts, *ACS Appl. Nano Mater.*, 2023, **6**(7), 5422–5433, DOI: **10.1021/acsanm.2c05555**.

64 S. Rojas-Buzo, P. García-García and A. Corma, Catalytic Transfer Hydrogenation of Biomass-Derived Carbonyls over Hafnium-Based Metal–Organic Frameworks, *ChemSusChem*, 2018, **11**(2), 432–438, DOI: **10.1002/cssc.201701708**.

65 S. Rojas-Buzo, P. García-García and A. Corma, Hf-Based Metal–Organic Frameworks as Acid-Base Catalysts for the Transformation of Biomass-Derived Furanic Compounds into Chemicals, *Green Chem.*, 2018, **20**(13), 3081–3091, DOI: **10.1039/c8gc00806j**.

66 M. J. Climent, A. Corma, V. Fornés, R. Guil-Lopez and S. Iborra, Aldol Condensations on Solid Catalysts: A Cooperative Effect between Weak Acid and Base Sites, *Adv. Synth. Catal.*, 2002, **344**(10), 1090–1096, DOI: **10.1002/1615-4169(200212)344:10<1090::AID-ADSC1090>3.0.CO;2-X**.

67 G. Li, B. Wang and D. E. Resasco, Oxide-Catalyzed Self- and Cross-Condensation of Cycloketones. Kinetically Relevant Steps That Determine Product Distribution, *J. Catal.*, 2020, **391**, 163–174, DOI: **10.1016/j.jcat.2020.07.019**.